

Even-denominator fractional quantum Hall physics in ZnO

J. Falson^{1,2}, D. Maryenko³, B. Friess⁴, D. Zhang⁴, Y. Kozuka¹, A. Tsukazaki^{5,6}, J. H. Smet⁴,
M. Kawasaki^{1,3}

¹ Department of Applied Physics and Quantum-Phase Electronics Center (QPEC), University of Tokyo, Tokyo 113-8656, Japan.

² Department of Advanced Materials Science, University of Tokyo, Kashiwa 277-8561, Japan.

³ RIKEN Center for Emergent Matter Science (CEMS), Wako 351-0198, Japan.

⁴ Max Planck Institute for Solid State Research, Heisenbergstrasse 1, D-70569 Stuttgart, Germany.

⁵ Institute for Materials Research, Tohoku University, Sendai 980-8577, Japan.

⁶ PRESTO, Japan Science and Technology Agency (JST), Tokyo 102-0075, Japan.

The follow sections act as supplementary details of content introduced in the main text. The data was gathered over three separate sample cool-downs.

1. Sample and measurement details
2. Examination of the Shubnikov-de Haas oscillations
3. Hysteric features at high T
4. Energy scales in the ZnO 2DES: electrons and composite fermions
5. Temperature dependent magnetotransport
6. Waterfall representation of tilt angle dependent transport data
7. Isotropy of the magnetotransport

1. Sample and measurement details

The MgZnO/ZnO heterostructure of charge density $n_e = 2.3 \times 10^{11} \text{ cm}^{-2}$ and zero-field mobility $\mu_e = 530,000 \text{ cm}^2/\text{Vs}$ was fabricated by molecular beam epitaxy³³ using Zn-polar single crystal ZnO substrates (Tokyo Denpa), 7N5 Zn and 6N Mg metallic sources and oxygen species provided from distilled liquid ozone (Meidensha). The growth temperature was $T_G = 750^\circ\text{C}$, and the Mg content is estimated to be roughly 1%. The liquid nitrogen cooled chamber has a base pressure of $1 \times 10^{-8} \text{ Pa}$, with the pressure rising to 10^{-5} Pa order during growth. Growth conditions were highly Zn rich with a Zn flux of $1 \times 10^{-3} \text{ Pa}$, as

measured by a beam flux monitor. The growth rate was 800nm/hour, with a film thickness of 300nm MgZnO/500nm ZnO. A roughly $4 \times 4 \text{ mm}^2$ chip was cut from the grown wafer and eight indium contacts were soldered at the sample edges. This system is observed to spontaneously form a 2DES in ZnO at the heterointerface, without the need for remote modulation doping or electrostatic gating. The width of the wavefunction within ZnO in the growth direction is estimated to be on the order of 5nm, as measured by capacitance experiments³⁴ and supported by numerical calculations³⁵. This is expected to lead to a relatively reduced coupling of the 2DES with an in-plane magnetic field compared to quantum wells (30 ~ 40nm in width) commonly used in GaAs heterostructures^{23,27,36} to investigate $\nu_e = 5/2$. In those systems, it is established that when the in-plane magnetic length becomes comparable to the 2DES width the stability of FQH states is significantly affected. Accordingly, in ZnO this effect is expected to be less acute. The magnetotransport studies were performed in van der Pauw geometry using low frequency lock-in techniques with an excitation current of 10 nA. The sample was loaded on a quasi-frictionless *in-situ* rotating stage in a top-loading-into-mixture dilution refrigerator with a base temperature $T < 20\text{mK}$ to allow for tilted field studies.

2. Examination of the Shubnikov-de Haas oscillations

A magnified view of the low field Shubnikov-de Haas oscillations is provided in Fig. S1. Minima corresponding to even filling factors are indicated by the red guide-line and odd by blue. The superior stability of odd filling factors when going to lower B suggests $E_z > E_{\text{cyc}}/2$, and hence LL of different orbital number to be closer than of the same. The occupation of two subbands can normally be detected as a beating in low field Shubnikov – de Haas oscillations. As shown in Fig. S1, such a signature is however absent both in the raw data as well as their Fourier transform (see inset), suggesting this degree of freedom does not exist in the system under investigation.

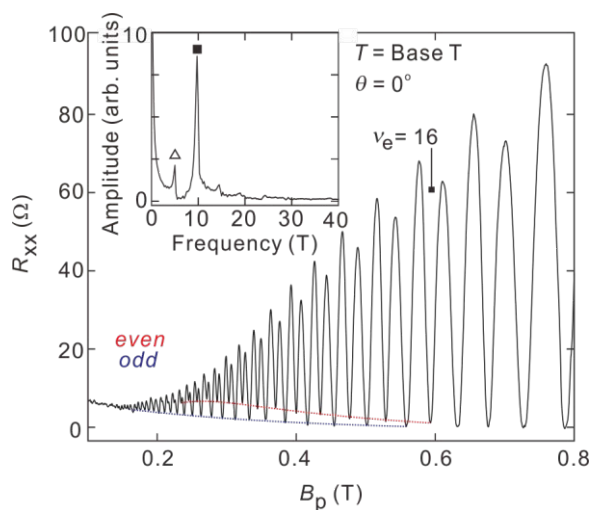


Figure S1: Magnification of low field Shubnikov-de Haas oscillations with minima at even (red) and odd (blue) filling factors indicated. Signatures of beating are absent. Inset: The Fourier transform of Shubnikov-de Haas oscillations reveals two primary single peaks corresponding to non-spin split (open triangle) and spin-split (solid square) oscillation frequencies. Weak harmonics are observed for higher frequencies.

3. Hysteric features at high T

At high $T = 600$ mK, the high resistance pocket observed on the flank of the $\nu_e = 2$ integer quantum Hall state displays sweep direction dependent hysteric magnetoresistance (sweep rate = 100 mT/min), as shown in Fig. S2. This behavior shares similarities to the resistance spikes observed in both our previous work³⁷ and in AIAs based 2DES, suggesting remnant magnetism due to spontaneous symmetry breaking in the vicinity^{24,25}.

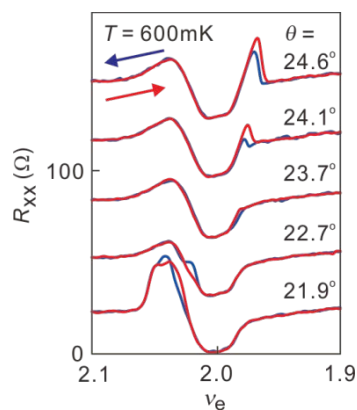


Figure S2: Sweep direction dependent transport at high $T \sim 600$ mK revealing hysteric features for intermediate tilt angles.

4. Energy scales in the ZnO 2DES

Electrons

Here we explore quantitatively the energy scales of electrons in the heterostructure under investigation. Firstly, the electron spin susceptibility, $g_e^*m_e^*/m_0$, is addressed through the observation of electron level coincidences as a function of increasing tilt.

Coincidence positions obey the relationship

$$\frac{g_e^*m_e^*}{2m_0 \cos(\theta)} = j_e$$

where θ indicates the tilt angle at which the coincidence occurs, and j_e is the index difference between the crossing electron LLs. Through the remainder of this section we simplify the notation by referring to m_e^*/m_0 as \bar{m}_e^* .

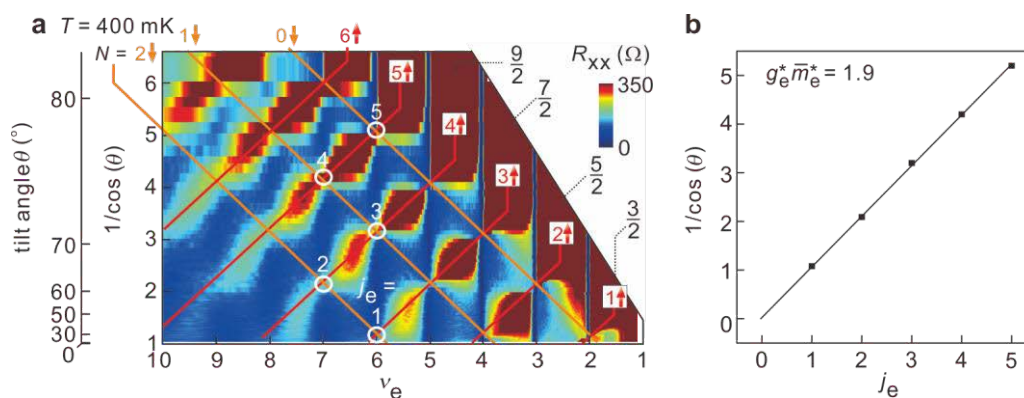


Figure S3: **a**, Magnetotransport data recorded at 400 mK as a function of filling factor and tilt angle. The Landau level number and spin orientation of the partially filled level at the chemical potential in the different low and high resistance regions are indicated by the red and orange lines. Some coincidence positions, characterized by the difference in the orbital index of the two levels involved, j_e , are indicated by white circles. **b**, $1/\cos(\theta)$ of the identified transitions as a function of j_e . The slope reflects the $g_e^*\bar{m}_e^*$ of the system.

The magnetotransport data used for this analysis are shown in Fig. S3a as a function of ν_e and θ . In this representation, distinct regions of ‘high’ and ‘low’ resistances are seen depending on the spin orientation of the partially occupied LL at the chemical potential. This is a

reproducible character of ZnO magnetotransport³⁸. The resistance is high (low) when the partially filled level possesses the majority (minority) spin orientation, *i.e.* spin up (down). The transitions between these cases are then interpreted as a level crossing, and some of these are marked by white circles in panel a. Here, note that the first LL coincidence position is evaluated at $\theta \sim 24^\circ$. The angle at which these transitions occur are plotted as a function of j_e in Fig. S3b. Enforcing a linear relationship passing through the origin between the j_e indices and $1/\cos(\theta)$, as described by the above expression, yields a value of $g_e^* \bar{m}_e^*$ equal to 1.9 as a best fit to the data. This magnitude of $g_e^* \bar{m}_e^*$ confirms that at zero tilt LL with opposite spin and different orbital index are closer to each other than opposite spin branches of one and the same LL. The ratio of enhancement, $g_e^* \bar{m}_e^*/g_b m_b^*$ equals 3.3, consistent with previous studies³⁷.

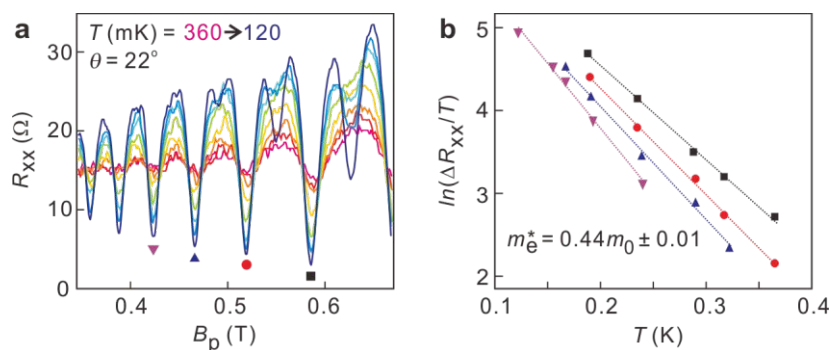


Figure S4: **a**, Temperature dependence of Shubnikov-de Haas oscillations. **b**, Analysis of the effective mass.

To determine the effective mass of electrons (m_e^*), the temperature dependence of low field Shubnikov de Haas (SdH) oscillations is investigated close to the first coincidence point of $\theta \sim 24^\circ$ as shown in Fig. S4. Here, spin split levels are nearly degenerate and therefore the damping of the SdH oscillations primarily reflects the cyclotron energy of the system, and hence effective mass. The analysis is performed using the following Dingle expression for temperature ranges where spin splitting is still not resolved:

$$\frac{\Delta R_{xx}}{R_0} = 4\chi \exp(-\pi/\omega_c \tau_q) / \sinh \chi$$

In this expression, $\chi = 2\pi^2 k_B T / \hbar \omega_c$ and $\omega_c = eB_p / m_e^*$.

The analysis yields a value $m_e^* = 0.44m_0 \pm 0.01$, consistent with previous work³⁹. This allows us to determine $g_e^* = 4.3$ and leads to a cyclotron energy of $E_{cyc} = 3.1B_p$ (K) and a Zeeman energy of $E_Z = 2.9B_t$ (K).

Utilizing these single particle energy levels we can anticipate what orbital character and physics (based on past GaAs experiments) is expected for each partial filling factor at zero tilt. The real observations of this work are noted in the right column.

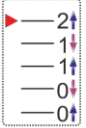



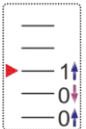

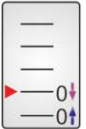

$\nu_e =$	Expected N_e and FQH effect ($\theta = 0^\circ$)	Observation in this work ($\theta = 0^\circ$)
9/2	2, No FQH effect, charge density waves 	Likely 1, Incipient FQH features 
7/2	1, Odd and even denominator FQH effect 	1, Odd and even denominator FQH effect 
5/2	1, Odd and even denominator FQH effect 	0, Robust odd denominator FQH effect 
3/2	0, Robust odd denominator FQH effect 	0, Robust odd denominator FQH effect 

Table S1: Summary of expected and observed behavior at half fillings of LL including level ordering schematics. Grey shaded panels represent the series observed in experiment.

Finally, we can quantify κ , the ratio of the Coulomb energy to the cyclotron energy from which the magnitude of Landau level mixing can be inferred in this system:

$$\kappa = \frac{E_{coulomb}}{E_{cyc}}$$

$$= \frac{e^2/4\pi\epsilon l_B}{\hbar e B_p / m_e^*}$$

Here, ε is the material's dielectric constant ($= 8.5$ in ZnO) and l_B is the magnetic length, $\sqrt{\hbar/eB_p}$. Table S2 summarizes the magnitude of key sample parameters. For all calculations, the measured effective mass $m_e^* = 0.44m_0$ has been used.

Electron spin susceptibility, $g_e^* \bar{m}_e^*$	1.9
Enhancement of spin susceptibility, $g_e^* m_e^* / g_b m_b^*$	3.3
Electron effective mass, m_e^*	$0.44m_0$
Electron g -factor, g_e^*	4.3
Landau level mixing, κ	16.5 @ $B_p = 2.1\text{T}$ ($\nu_e = 9/2$) 14.5 @ $B_p = 2.7\text{T}$ ($\nu_e = 7/2$) 9.7 @ $B_p = 6.2\text{T}$ ($\nu_e = 3/2$)
Transport scattering time τ_{tr}	~ 130 ps
Quantum scattering time, τ_q	~ 8 ps
Wigner-Seitz radius, r_s	11.6

Table S2: Summary of key sample parameters.

Composite fermions

We may quantify the effective mass of CF (m_{CF}^*) via two methods – analyzing the damping of oscillations centered on $\nu_e = 3/2$ through the analogy of Shubnikov-de Haas oscillations of CF, or alternatively by activation energy measurements in Fig. S5. For the latter method, the data used for this analysis is presented in Fig. S10, where the rotation angle $\theta = 0^\circ$.

Shubnikov-de Haas analysis:

Previous studies have focused on CF at $\nu_e = 1/2$ and the oscillations centered there^{39,40,41}. Here, we in analogy analyze the oscillations centered on $\nu_e = 3/2$. The amplitude of oscillations is analyzed according to the Dingle expression:

$$\frac{\Delta R_{xx}}{R_0} = 4\chi \exp(-\pi/\omega_{CF}\tau_q) / \sinh\chi$$

Where $\chi = 2\pi^2 k_B T / \hbar \omega_{CF}$ and $\omega_{CF} = eB_{eff} / m_{CF,SdH}^*$ now includes the CF effective mass, and represents the energy separation between CF levels in the effective magnetic field B_{eff} . The result of this analysis for strong fractional states is shown in Fig. S5. Focusing on the $x/3$ and $x/5$ states, the mass is seen to increase linearly through the relationship:

$$m_{CF,SdH}^* = 1.3m_0 + 0.1B_{eff}$$

This allows us to estimate the effective mass at filling $3/2$ when $B_{eff} = 0$: $m_{CF,3/2}^* = 1.3 m_0$. We note that the $x/7$ states deviate from this relationship. This may reflect the development of divergent behavior when approaching half filling, as seen in previous works^{40,41}.

Activation energy analysis:

An alternative means for estimating the effective mass of composite fermions is the determination of the cyclotron energy gap through an activation energy analysis for the fractional states. The temperature dependent transport is shown in Fig. S10. The activation energy can be written as:

$$\Delta = \hbar \omega_{CF} - \Gamma = \hbar e B_{eff} / m_{CF}^* - \Gamma$$

Here, Γ is a measure of the disorder. The analysis is shown in the bottom panel of Fig. S5. A roughly linear dependence of the activation energy of fractional states is seen to emanate from $\nu_e = 3/2$ with a negative intercept of Γ . The slope represents the increasing cyclotron gap of composite fermions with increasing B_{eff} and allows the extraction of the effective mass. It is found to be $1.1 m_0$ for negative B_{eff} and $1.7 m_0$ for positive B_{eff} . These values are in reasonable agreement with the values gained from the previous Dingle analysis.

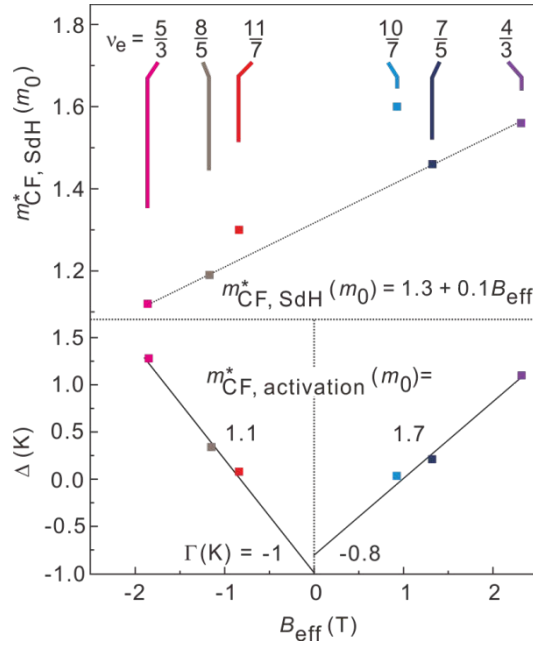


Figure S5: Analysis of the CF effective mass around $\nu_e = 3/2$. Top: Mass as derived from a Dingle plot analysis of the CF Shubnikov-de Haas oscillations. Bottom: Mass as derived from an analysis of the activation energy.

CF coincidences and $g_{CF}^* \bar{m}_{CF}^*$ (Fig. S6, S7 and S8)

As can be seen from the magnetotransport data presented in Fig. 4 of the main text, the resistance of the minimum of odd-denominator FQH states oscillates with modifying the tilt angle. Line traces of each FQH state minimum are shown in Fig. S6e. Local resistance maxima are indicated by bars above each curve with the bar size corresponding to the estimated error in assignment. Pronounced minima are also highlighted. This behavior can be associated with the crossing of CF levels. Analogous to what occurs for electrons in integer quantum Hall states, these maxima are attributed to the intersection²⁸ of levels of two CF Landau fans (panel c,d), which emanate from the electron LL (panels a,b) ($N_e = 0, \downarrow$) and ($N_e = 1, \uparrow$), when moving away from exactly $\nu_e = 3/2$. In the remainder, these levels are referred to as A and B , respectively. In Fig. S6c and d (blue outline panels), the intersecting fans are drawn schematically for negative and positive values of ΔE . The orbital quantization energy controlling these CF energy levels equals $(N_{CF} + \frac{1}{2}) \cdot \hbar\omega_{CF,X}$. Here, $\hbar\omega_{CF,X} = \frac{\hbar e B_{eff}}{m_{CF,X}^*}$ with $m_{CF,X}^*$ the mass of CF and $B_{eff} = 3 \cdot (B_p - B_{p,3/2})$ the effective magnetic field CFs experience away from $\nu_e = 3/2$. The orbital index of CF levels emanating from the fan

associated with electron level A and B are denoted by level index A_{CF} and B_{CF} , running $0,1,2,\dots$ etc. The spin of CFs is inherently that of the host electron LL. Since the orbital index of the underlying electron level differs, the composite fermions occupying the two different CF fans may possess a different mass. This has been taken into account by adding the label X to $m_{CF,X}^*$ and $\hbar\omega_{CF,X}$. Levels exchange position whenever the energy difference ΔE between the electron levels A and B equals the difference in the orbital quantization energy of the CF levels:

$$\Delta E = A_{CF} \cdot \hbar\omega_{CF,A} - B_{CF} \cdot \hbar\omega_{CF,B} \quad (1).$$

For unequal effective masses of the two CF level fans, the number of available degrees of freedom in this equation to fit the experimental data and coincidences hampers a convincing identification of the quantum numbers of the levels involved at each crossing. In the remainder, we will assume identical CF effective masses. Even though this assumption cannot be justified *a priori*, it simplifies the analysis considerably and, as will be seen, still improves our understanding.

As evident from Eq. 1 assuming $\hbar\omega_{CF,A} = \hbar\omega_{CF,B} = \hbar\omega_{CF}$, all the crossing points for a fixed level index difference $j_{CF} = (A_{CF} - B_{CF})$ should fall on a line when plotted in the (B_p, B_t) -plane. We note that for unequal CF effective masses contours of constant j_{CF} are curves rather than lines. In addition, strictly speaking the CF effective mass is not constant, but scales with the Coulomb interaction strength and hence also the square root of the perpendicular magnetic field. This too causes a deviation of contours of constant j_{CF} from a straight line. However the mass correction across the relevant range of fields is small. It will be ignored for the moment and revisited below. These lines for different values of j_{CF} should all pass through a common point located at $B_p = B_{p,3/2}$ where B_{eff} and $\hbar\omega_{CF}$ equal 0 and a B_t for which $\Delta E = 0$, i.e. for which the electron LL A and B swap positions.

When p CF levels are completely filled, the electron system condenses in a FQH state. Here, the series of fractional quantum Hall states will be described by $\nu_e = 1 + \frac{p}{2p \pm 1}$, since the lowest spin up level of $N_e = 0$ is energetically separated. This is in contrast to previous works²⁸ which utilize $\nu_e = 2 - \frac{p}{2p \pm 1}$. For the assignment chosen here, filling $\nu_e = 4/3$

corresponds to one completely filled composite fermion Landau level, whereas at $\nu_e = 5/3$ two such levels are completely populated. Experimental evidence supporting this particular assignment is discussed below in conjunction with Fig. S8. For fractional quantum Hall states corresponding to p completely filled composite fermion levels, we will approach a number of level crossings as ΔE is altered by tilting the sample. In Fig. S6c,d we have set $p = 4$ for illustrative purposes and display two different instances for positive and negative ΔE . At the level crossing, the state undergoes a discrete shift in the ratio of occupied CF levels $A_{CF}:B_{CF}$ (insert schematic of Fig. S6.c,d).

When electron level A has not crossed electron level B , i.e. $\Delta E > 0$, j_{CF} is larger than zero when a level crossing occurs. In general level coincidences will be either away from or at the Fermi energy. For $j_{CF} \geq p$, the coincidences always occur above the Fermi energy and they should only affect R_{xx} weakly or not at all for these tilt angles. For $0 < j_{CF} < p$ there are level coincidences at or below the Fermi energy. Two cases can be distinguished. If p is odd (even), the Fermi level will be in a gap for coincidences with j_{CF} odd (even) and a deep minimum in the longitudinal resistance is expected. In contrast, if j_{CF} is even (odd), the Fermi level will be located at the coincidence instead resulting in a breakdown of the quantum Hall effect and a maximum in R_{xx} can be expected. In Table S3 we summarize the crossing events for different values of p and j_{CF} and classify them according to whether they appear at, above or away (i.e. below and above) from the Fermi energy. The thick line running through this table demarcates the boundary below which coincidences only occur above the Fermi energy. For one specific value of $p = 4$, we illustrate the classification of the coincidences for different values of j_{CF} with energy level diagrams.

The above considerations provide important guidelines for assigning the features marked in Fig. S6e to specific contours of constant j_{CF} . To this end the features are plotted in the (B_p, B_t) -plane in Fig. S7. The following criteria serve as an assessment of the quality of the fit:

- for a constant j_{CF} index line, the series of coincidences should oscillate between strong/weak, corresponding to transitions at/below the chemical potential. The strong minima in the longitudinal resistance are labelled by red squares in Fig. S6e and S7.
- a complete breakdown of the fractional quantum Hall state must be associated with a transition at the chemical potential.

In order to obtain a reasonable agreement between the data and expression (1), the following assumptions are adopted:

- $\frac{g_{CF}^* m_{CF}^*}{m_0} = g_{CF}^* \bar{m}_{CF}^*$ is constant for each line of constant j_{CF} , but is allowed to fluctuate between the different lines.
- The origin ($B_{eff} = 0$) is free to fluctuate between lines.

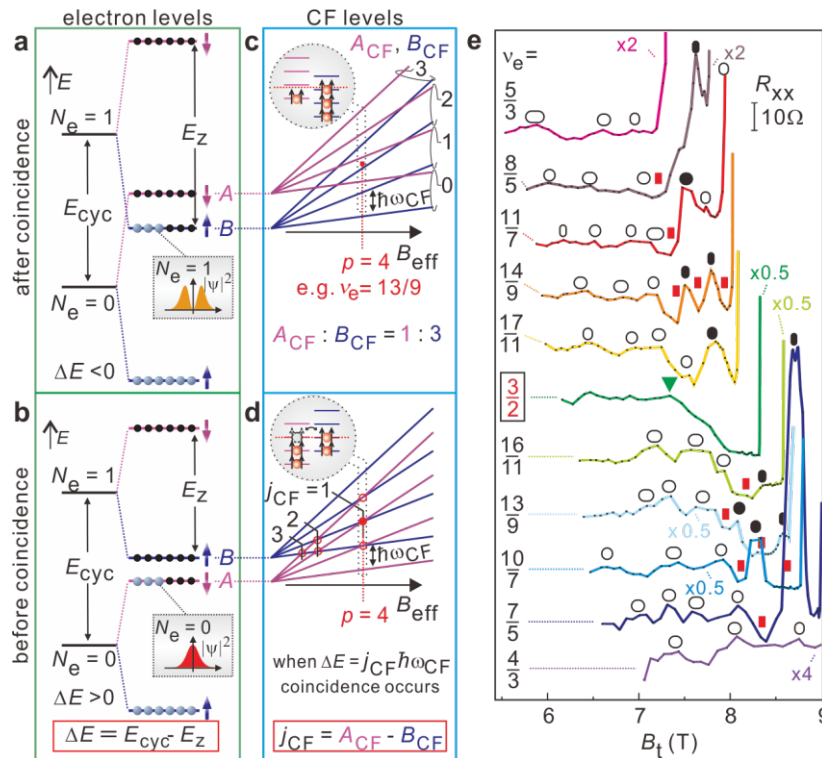


Fig. S6: **a & b**, Schematic of electron LL (green outlined panels) sequence after and before coincidence. The insets schematically show the differing wave function between $N_e = 0$ and 1. **c & d**, Intersecting CF level fans (blue outlined panels) of the corresponding electron LLs A and B . When p (here 4 for illustrative purposes) CF LLs are completely filled the FQH effect arises. **e**, Tracking of the minima of FQH states centered on $\nu_e = 3/2$ for base temperature. Strong local maxima are indicated by black bars with weak local maxima by white bars. Strong minima noted by red boxes (see text). Scaling factor of each resistance trace is indicated by colored tags.

$v_e =$	5/3	8/5	11/7	14/9	17/11	16/11	13/9	10/7	7/5	4/3
$p =$	2	3	4	5	6	5	4	3	2	1
$j_{CF} = -1$	○	X	○	X	○	X	○	X	○	X
0	X	○	X	○	X	○	X	○	X	○
1	○(s)	X	○	X	○	X	○	X	○	X
2	X	○(s)	X	○	X	○	X	○	X	X
3	X	X	○(s)	X	○	X	○	X	X	X
4	X	X	X	○	X	○	X	X	X	X
5	X	X	X	X	○	X	X	X	X	X
6	X	X	X	X	X	X	X	X	X	X
7	X	X	X	X	X	X	X	X	X	X
8	X	X	X	X	X	X	X	X	X	X

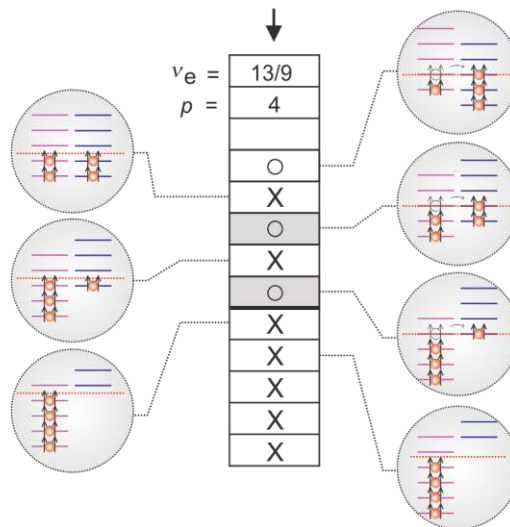


Table S3: Summary of expected spin transitions according to the model presented. Circles correspond to transitions expected at the Fermi energy. Crosses (X) correspond to level crossings away from the Fermi energy. Shaded squares represent strong features which are observed in the experimental transport data at the assigned j_{CF} index position. The marker “(s)” Signifies spikes identifiable in transport at intermediate temperatures (see Fig. S8). The bold line marks the condition below which all transitions correspond to those above the Fermi energy. The bottom set of level diagrams schematically display the evolution of transitions for $p = 4$ with changing j_{CF} when gradually shifting CF occupation between A and B levels.

These two final assumptions are not described by the simple schematic representation in Fig. S6. However, only with their inclusion the data points may be fit effectively, as per Fig. S7. Tracking each j_{CF} index line, transitions may be seen to indeed oscillate between strong/weak, corresponding to transitions at/below the chemical potential. A good agreement is achieved supporting our assignment of the transitions. An alternative representation of the fit is shown in Fig. S8, where the j_{CF} lines are overlaid on the transport presented in Fig. 4 of the main text. For the sake of completeness we do note that the fitting procedure is complicated somewhat by the fact that some features in R_{xx} associated with levels crossings are more apparent at

intermediate temperatures. A few discrete traces are shown in Fig. S8b where $T \sim 30$ mK. They reveal a resistance spike in the $\nu_e = 5/3$ minimum ($\theta \sim 32.5^\circ$), but not for $\nu_e = 4/3$. This *a posteriori* confirms the assignment of the series of FQH states being described by $\nu_e = 1 + \frac{p}{2p \pm 1}$ and $\nu_e = 5/3$ corresponding to a $p = 2$ filling, since only for this assignment a single level crossing with $j_{CF} > 0$ is expected at the chemical potential for $\nu_e = 5/3$ and none for $\nu_e = 4/3$.

As pointed out previously within the composite fermion model the effective mass of the quasiparticles should depend on the strength of the Coulomb interaction⁴², resulting in the relationship $m_{CF}^* \propto \sqrt{B_p}$. In Fig. S7 and S8 we have included such a dependency into the $g_{CF}^* \bar{m}_{CF}^*$ term used to describe each j_{CF} coincidence position as dotted lines. In this fit, the magnitude of $g_{CF}^* \bar{m}_{CF}^*$ is renormalized relative to half filling, $g_{CF}^* \bar{m}_{CF}^* \propto \sqrt{B_p} / \sqrt{B_{p,3/2}}$. This procedure evidently does not change the j_{CF} indices resulting from the fitting procedure as the difference in Coulomb interaction strength over the magnetic fields probed (5.5 T $< B_p < 6.9$ T) is only of the order of 10% of the total and such difference is within the bounds of experimental error in determining the points of coincidence.

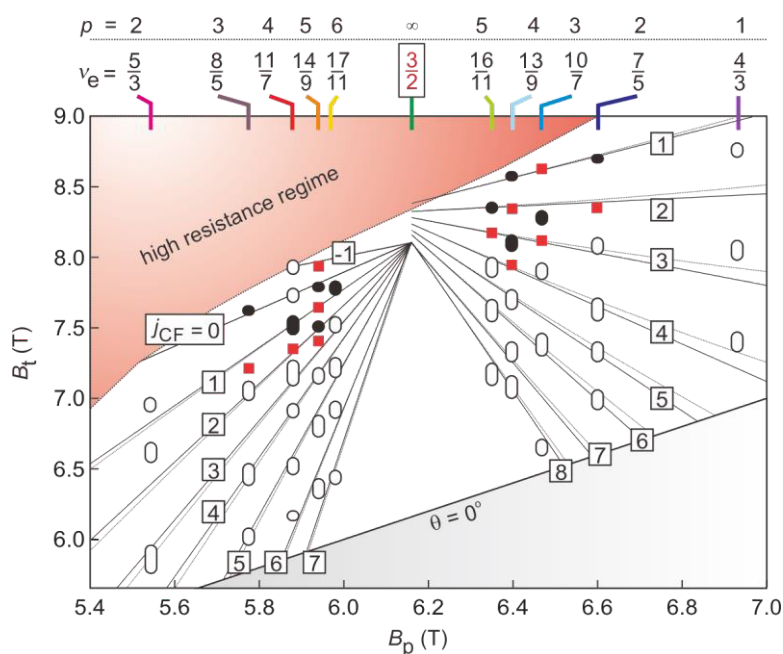


Fig. S7: Mapping of the local maxima in the (B_p, B_t) -plane for prominent FQH states. j_{CF} index lines are overlaid. The solid lines do not include the magnetic field correction to the CF effective mass, whereas the dotted lines do. Black data points correspond to strong features in magnetotransport. Red points correspond to strong minima. White data points correspond to weak features in R_{xx} .

j_{CF}	$\nu_e > 3/2$	$\nu_e < 3/2$
-1	8.6	-
0	-	-
1	8	10
2	8.2	10
3	8.2	9.4
4	8.2	9
5	7.4	9
6	6	9
7	5.6	8.6
8	-	8.4

Table S4: Summary of values of $g_{CF}^* \bar{m}_{CF}^*$ used as slopes for j_{CF} index lines.

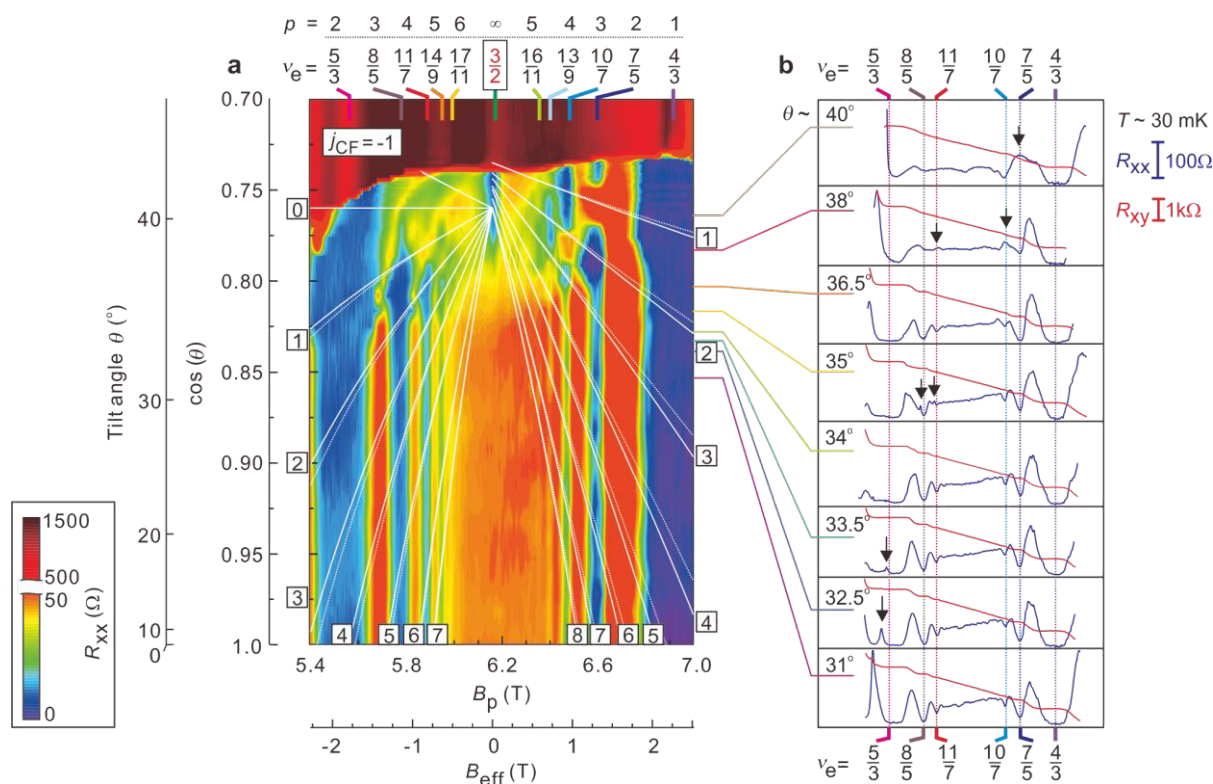


Fig. S8: **a**, Magnetotransport mapping (as shown in Fig. 4 of main text) around $\nu_e = 3/2$ with the j_{CF} index transitions lines overlaid (solid lines without field correction, dotted lines with field correction to the CF effective mass). **b** Intermediate temperature ($T \sim 30$ mK) magnetotransport for discrete tilt angles with level crossing events highlighted by black arrows. These are enforced to correspond to level crossings at the chemical potential in the fitting procedure.

This fitting procedure allows the assignment of a j_{CF} index for all transitions observed. Using this index inferred from the fit, it is possible to quantify $g_{CF}^* \bar{m}_{CF}^*$ for each state across the transitions. A crossing occurs with an index difference j_{CF} between the two CF spin-split ladders emanating from the electron levels A and B under the condition,

$$-g_{CF}^* \bar{m}_{CF}^* \cdot B_t = j_{CF} \cdot 6m_0 \cdot (B_p - B_{p, \frac{3}{2}}) - \frac{2m_{CF}^* m_0}{m_e^*} \cdot B_p, \quad (2)$$

It allows extracting $g_{CF}^* \bar{m}_{CF}^*$ for every FQH state of filling p by plotting the B_t/B_{eff} values at which a level coincidence for this filling is observed in experiment as a function of j_{CF} . This has been done in Fig. S9 using the data in Fig. 4 of the main text and the transitions identified in Fig. S6 and S7. The slope of the linear fit to these data points for a given filling yields $g_{CF}^* \bar{m}_{CF}^*$, since all other quantities in the above expression are known. The final term determines only the offset, and is discarded in the analysis performed. The plotting of the data reveals two distinct slopes between data points across the set of transitions.

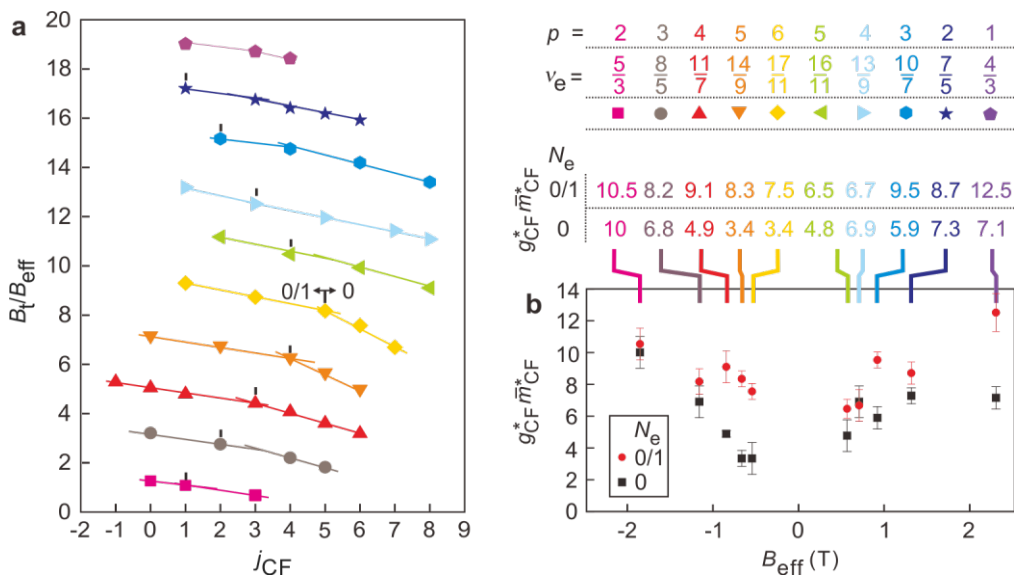


Figure S9: **a**, B_t/B_{eff} as a function of coincidence index, j_{CF} for spin transitions of odd denominator FQH states. Points for different filling factors are vertically offset for visual clarity. Vertical black lines indicate the crossover between states mixed in $N_e = 0$ & 1 (left hand side) and fully polarized in $N_e = 0$ (right hand side). Two indicative linear slopes for these two regimes are shown. This slope reflects $g_{CF}^* \bar{m}_{CF}^*$, as per the equation. **b**, $g_{CF}^* \bar{m}_{CF}^*$ as a function of B_{eff} for prominent FQH states for transport fully polarized in $N_e = 0$ (black squares) and mixed in $N_e = 0$ & 1 (red circles). The table summarizes the numerical results of $g_{CF}^* \bar{m}_{CF}^*$.

Discussion:

- Under the assumptions used in this analysis, it can be seen that the origin of j_{CF} lines for positive and negative B_{eff} is different. Moreover, a single origin for positive B_{eff} may not be determined. This cannot be explained by the simple model invoked here. It suggests that a parameter, either ΔE , g_{CF}^* or m_{CF}^* is changing as a function of tilt or polarization. All lines are however seen to converge close to where the $3/2$ state is observed. We note that in a two-component ground state scenario, these two electron spin levels may potentially form the two degrees of freedom required for the ground state.
- We note that the activation energy measurements performed above yield an estimate of the activation mass of CF, which has been shown theoretically to differ from that polarization mass of CF⁴². Knowing that $g_e^* \sim 4.3$ and that this is the same for CF, the measured $g_{CF}^* \bar{m}_{CF}^*$ also allows us to infer a value for the effective mass of CF from spin transitions, which is roughly $m_{CF}^* \approx 1.5 m_0$ when the transport is polarized in $N_e = 0$. Coincidentally, we find the values gathered from spin transitions to be of similar magnitude to the activation mass (which too probes fully polarization in $N_e = 0$ at $\theta = 0^\circ$).
- The analysis in Fig. S9 shows that $g_{CF}^* \bar{m}_{CF}^*$ is enhanced when rotating to higher tilt angles, or going to lower j_{CF} index transitions. This is entirely consistent with transport occurring in the $N_e = 1$ LL, where the stability of odd denominator states is severely reduced (or alternatively the mass gets larger). This behavior is clearly observed in Fig S9 where the slope of the linear interpolations differs depending on whether the system is mixed in $N_e = 0$ & 1 (left hand side of vertical line) or polarized in $N_e = 0$ (right hand side of vertical line). This behavior is also reflected in the activation energy analysis performed in Fig. 3c of the main text, where the $x/3$ and $x/5$ states significantly weaken after spin transitions to $N_e = 1$ nature occur. The enhancement of $g_{CF}^* \bar{m}_{CF}^*$ from this analysis is on the order of 50%.
- It is important to recognize that this is a common feature of odd-denominator states. This can be clearly seen in Figs. 1c and 4 of the main text where the $x/11$ and $x/9$ FQH states disappear as the $3/2$ -state emerges. This is particular noticeable on the low field side of $\nu_e = 3/2$, where the analysis suggests that the $j_{CF} = 0$ transition occurs (*i.e.* electron LL swap position). Here, besides $\nu_e = 5/3$, no other odd-denominator state exists. This is however entirely conducive with transport in $N_e = 1$.

- For the $\nu_e = 5/3$ state where $p = 2$, we see a transition in the activation energy for the $j_{CF} = -1$ transitions as detailed in the main text. In addition however, we see weak features in the longitudinal resistance close to $j_{CF} = 3$ and 0 where the model suggests that there is no crossing occurring at the chemical potential. We speculate this behavior to be the result of mixing of these energy levels due to the large coulomb energy in the system. Similar features were also observed in previous studies²⁸ and at other filling factors in this study. In agreement with expectations, for the $x/3$ states there is no drastic change in the activation energy when passing through such transitions. As stated above, maximizing the agreement between the strong/weak transitions at/below the chemical potential is a requirement of the fitting procedure.
- Due to the weak nature of these transitions, it is difficult to determine the exact magnetic field for higher j_{CF} index transitions and an error in quantifying $g_{CF}^* \bar{m}_{CF}^*$ inevitably will occur. This is compounded by the limited number of data points at the $x/3$ states. To minimize this error, the slope of the linear interpolation between points corresponding to transitions fully polarized in $N_e = 0$ and mixing in $N_e = 0$ & 1 is used for the analysis, rather than the spacing between individual transitions. This yields two notably different slopes. The error has been estimated in Fig. S9b for each regime independently. Where there are only two points in the interpolation (*i.e.* for the $x/3$ states), an error of 10% has been included as a rough estimate.
- We highlight other works which describe coincidence events between CF levels originating from different subbands in a GaAs wide quantum well⁴³ and valleys in AlAs⁴⁴.

5. Temperature dependent magnetotransport

In this section we explore the temperature dependence of the magnetotransport properties around various even-denominator fractional filling factors. These data sets allow the quantification of the energy gaps (Δ) of FQH states using the relationship $R_{xx} = e^{-\Delta/2k_B T}$. The error in quantification is expected to be on the order of $\pm 10\%$. The temperature is read from a calibrated Ruthenium Oxide thermometer located within the mixing chamber.

$\nu_e = 3/2$, $\theta = 0^\circ$ (Fig. S10)

The data collected around $\nu_e = 3/2$ at zero tilt were used in section 3 to analyze the effective mass of CF. These are plotted in Fig. S10.

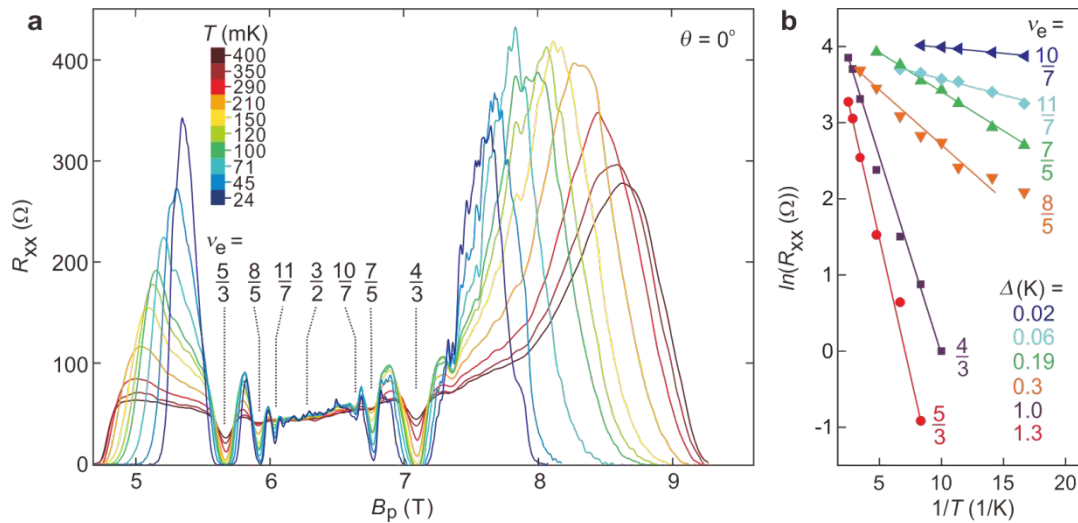


Figure S10: **a**, Temperature dependence of the magnetotransport around $\nu_e = 3/2$ at zero tilt. **b**, Activation energy analysis of FQH states.

$\nu_e = 3/2$, *Quantized regime* $\theta = 42^\circ$ (Fig. S11)

The magnetotransport data recorded at a tilt angle of $\theta = 42^\circ$, where the $\nu_e = 3/2$ state is fully developed and exhibits a quantized Hall resistance, are plotted in Fig S11. This tilt angle is close to the high-resistance regime, whose onset may be seen around $B_p \approx 5.7$ T.

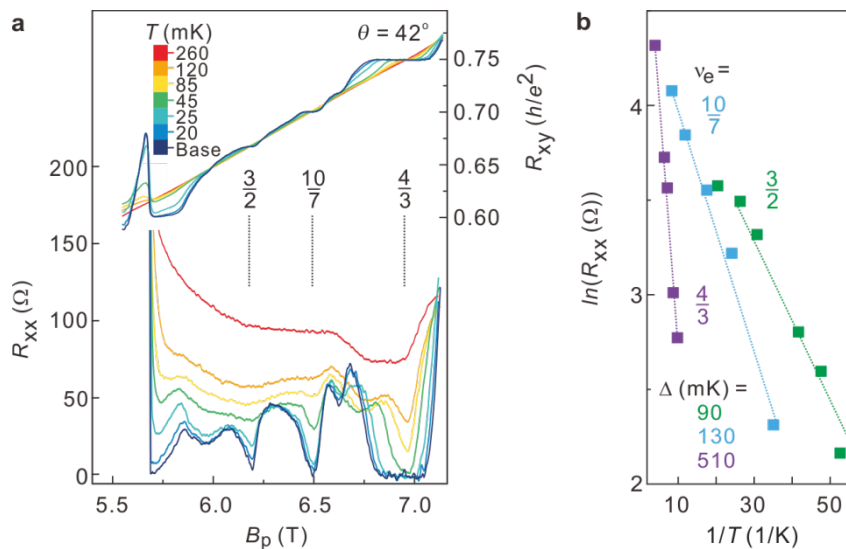


Figure S11: a, Temperature dependent magnetotransport around $\nu_e = 3/2$ at a tilt angle of $\theta = 42^\circ$, where the $\nu_e = 3/2$ state exhibits a quantized Hall resistance. **b,** Activation energy analysis of FQH states.

$\nu_e = 3/2$, *High resistance regime* $\theta = 45^\circ$ (Fig. S12)

At high tilt $\theta \gtrsim 42^\circ$ the system turns much more resistive. This is accompanied by the appearance of reentrant quantum Hall behavior as seen in Fig. S12. Temperature dependent magnetotransport around $\nu_e = 3/2$ is shown in Fig. S12. While minima at the most prominent fractional filling factors exist, robust reentrant integer quantum Hall behavior is observed in R_{xy} at low T . As a result the unambiguous identification of FQH states in this regime is not feasible.

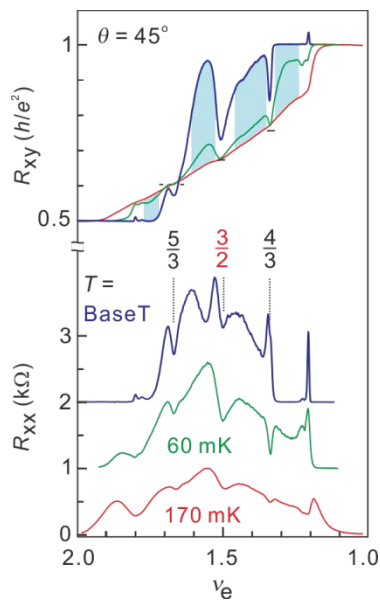


Figure S12: Temperature dependent magnetotransport around $\nu_e = 3/2$ at a tilt angle of $\theta = 45^\circ$. Developing reentrant integer quantum Hall states in R_{xy} are shaded light blue.

$\nu_e = 5/2$, $\theta = 0^\circ$ (Fig. S13)

Based on the $T = 400$ mK transport data in Fig. 2b, we conclude that for $\nu_e = 5/2$ at zero tilt the partially filled level belongs to the lowest LL and hence a compressible CF sea forms at $B_{\text{eff}} = 0$, analogous to around $\nu_e = 3/2$ at low tilt angle. Odd-denominator states may yield an estimate of the effective mass of CF in Fig. S13. For negative B_{eff} , $m_{CF,\nu=5/2}^* = 2.6m_0$. This

temperature dependent transport reveals also new information about the asymmetry of FQH states observed around $\nu_e = 5/2$. At $T \sim 50$ mK it is seen that a lone re-entrant integer quantum Hall state develops, on the high field side of half filling. The bulk becomes incompressible and the resistance drops to zero at base T .

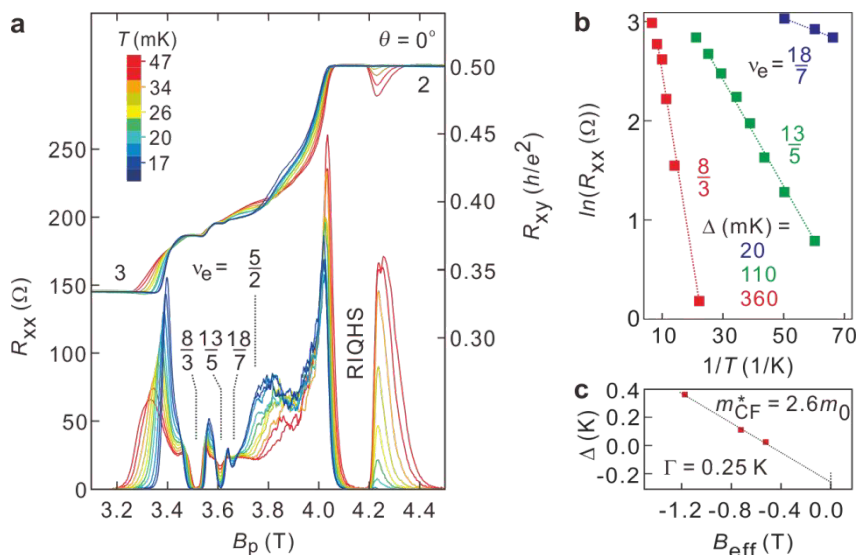


Figure S13: **a**, Temperature dependence of magnetotransport around $\nu_e = 5/2$. **b**, Activation energy analysis of FQH states. **c**, Analysis of the activation energy of odd-denominator FQH states enabling the determination of the CF effective mass.

$\nu_e = 7/2$, $\theta = 0^\circ$ (Fig. S14)

The temperature dependence of the longitudinal resistance at $\nu_e = 7/2$ and surrounding FQH states is shown in Fig. S14. Consistent with observations in GaAs 2DES for the $5/2$ state, FQH states are observed also at $x/3$, while being significantly weakened compared to the $x/3$ states in the lowest LL^{26,27}. Also similar to the common observation of $N_e = 1$ FQH states in GaAs, we find that the $3 + 1/3$ state is more robust than the $3 + 2/3$ state^{10,27}.

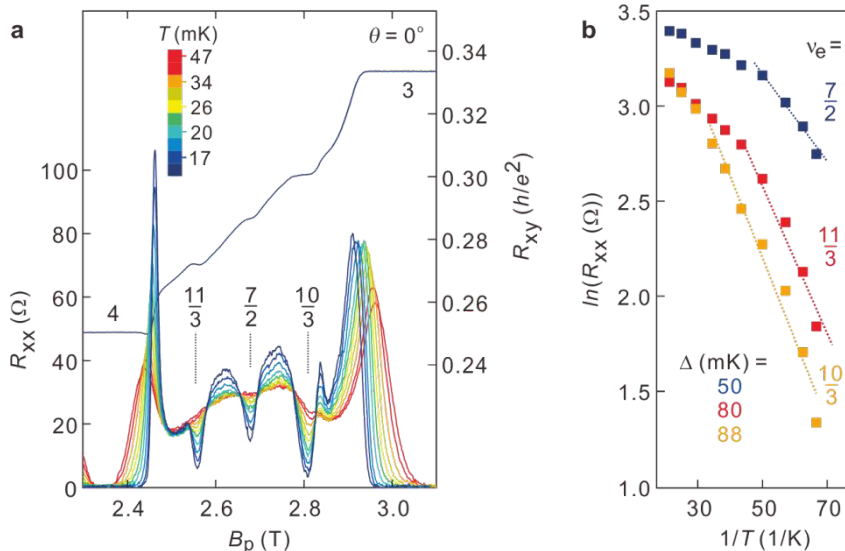


Figure S14: Temperature dependence of $\nu_e = 7/2$. **a**, Temperature dependent magnetotransport data. **b**, Activation energy analysis of FQH states.

$\nu_e = 9/2, \theta = 0^\circ$ (Fig. S15)

The temperature dependent magnetotransport around $\nu_e = 9/2$ is displayed in Fig. S15. The behavior here is different from that of the other partial filling factors presented above. While indeed at lower temperature, minima in the longitudinal resistance at rational fractional filling factors become more distinct, the absolute value of the minima is seen to rise when lowering the temperature. For the Hall resistance, plateau-like features form for these filling factors, but their values do not correspond to the values expected from a properly quantized state. Moreover, the Hall resistance shows temperature dependence. These observations prohibit conclusive identification of these states in this heterostructure.

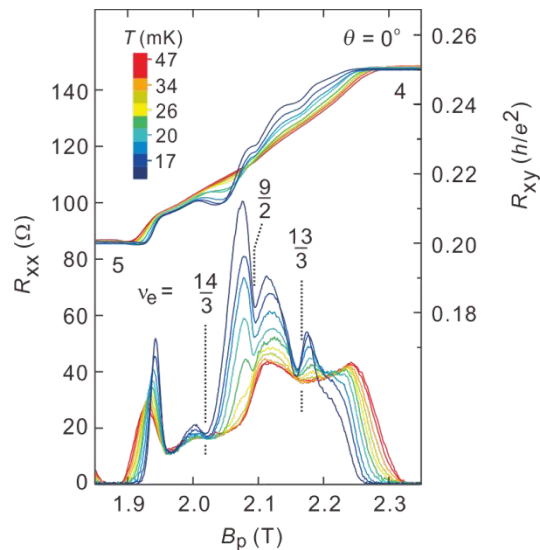


Figure S15: Temperature dependence around $\nu_e = 9/2$. The magnetic field corresponding to rational fractional filling factors are highlighted by vertical lines.

Summary of activation energies (Fig. S16)

A summary of all activation energies quantified in this section is provided in Fig. S16. Here, we plot the activation energies in units of Coulomb energy ($e^2/\epsilon l_B$) where $\epsilon = 8.5$ in ZnO, e is the elementary charge, and l_B the magnetic length ($= \sqrt{\hbar/eB_p}$).

We note that the activation energy of the $7/2$ state and $3/2$ state are $4.1 \times 10^{-4} e^2/\epsilon l_B$ and $4.5 \times 10^{-4} e^2/\epsilon l_B$, respectively, comparable to that of single component states reported in modest mobility AlGaAs/GaAs heterostructures²³ but an order of magnitude smaller than for the highest quality GaAs samples²⁷.

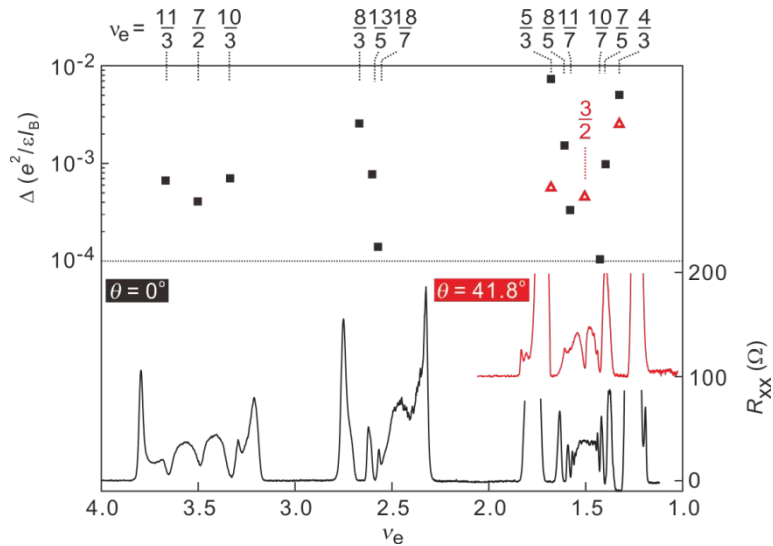


Figure S16: Magnetotransport (bottom) and summary of activation energies for filling factors identified in the text (top) as a function of filling factor for $\theta = 0^\circ$ (black trace, solid squares) and 41.8° (red trace, open triangles).

6. Waterfall representation of tilt angle dependent transport data

The transport for $7 > \nu_e > 2$ is shown in Fig S17. The $\nu_e = 7/2$ state remains robust up until the first coincidence position which occurs between the plots of $\theta = 21.4^\circ \sim 27.8^\circ$, from where the chemical potential ceases to be pinned in a $N_e = 1$ level. In contrast, the $\nu_e = 9/2$ minimum is seen to collapse by $\theta \sim 11^\circ$.

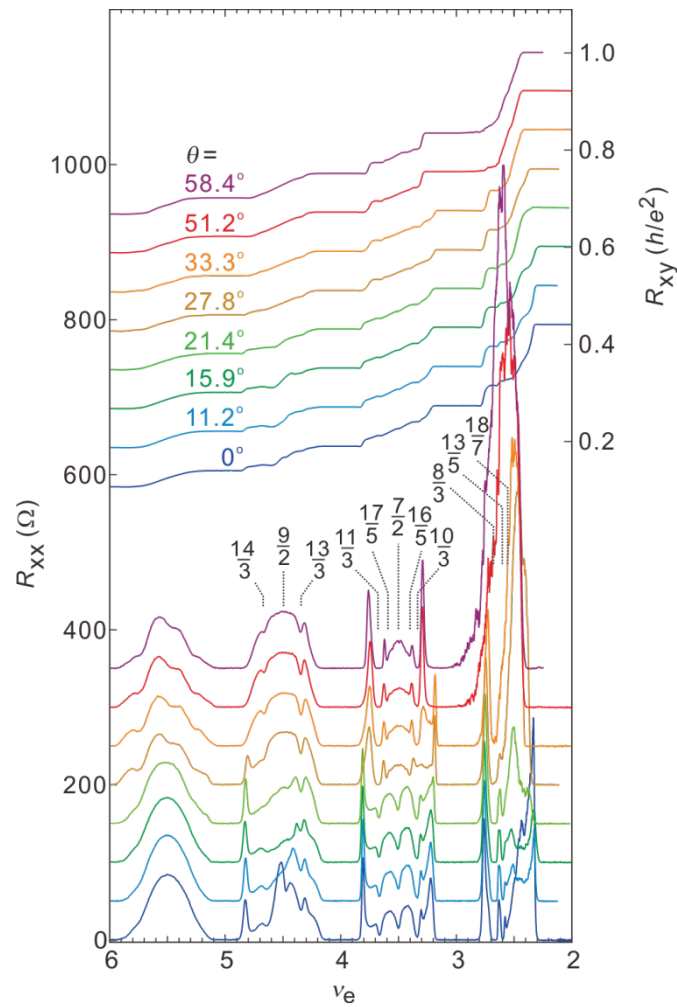


Figure S17: Higher LL magnetotransport data as a function of filling factor for $7 > \nu_e > 2$ for increasing tilt angles.

Waterfall plots of the magnetotransport data presented as 2D color renditions in the main text are displayed in Figs. S18 and S19. The tilt angle for respective traces is indicated by the colored tag.

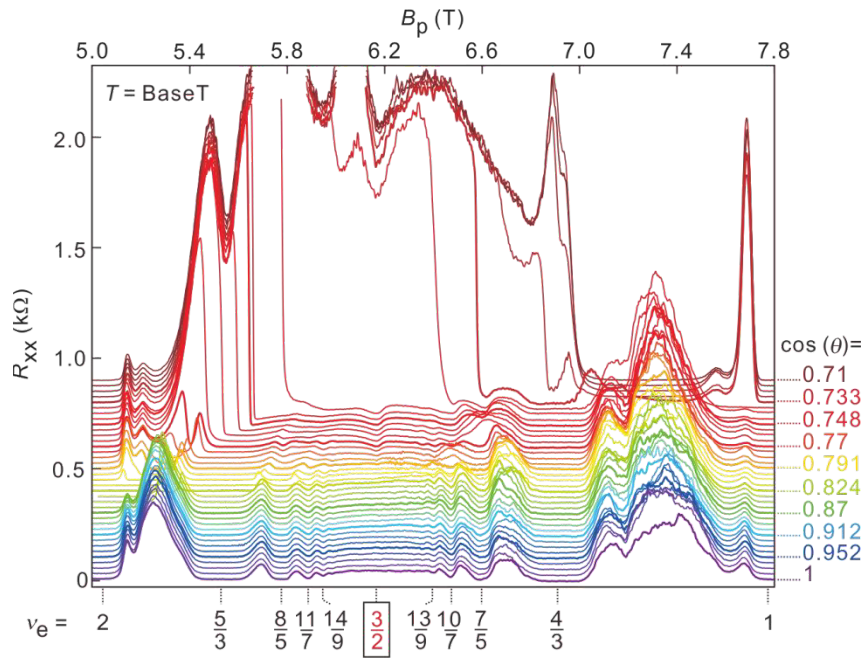


Figure S18: Waterfall plots of representative base temperature data shown as a color rendition in Fig. 4 of the main text.

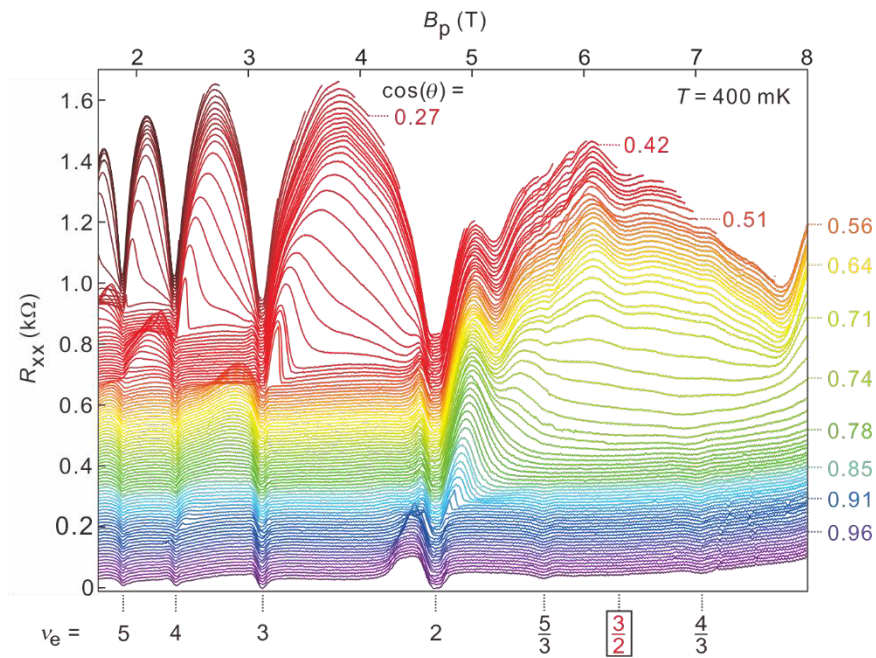


Figure S19: Waterfall plot of the 400 mK data in Fig. 2b of the main text.

7. Isotropy of the magnetotransport

In high mobility AlGaAs/GaAs heterostructures, it is known that transport in higher index LLs ($N_e \geq 2$, $\nu_e > 4$) is dominated by anisotropic features associated with the formation of coulomb interaction mediated charge density wave ground states¹⁸⁻²⁰. We notice a distinct absence of such anisotropy in the ZnO system under all configurations, despite the square van der Pauw geometry used here, which is known to amplify the transport anisotropy⁴⁵. To illustrate this, the current is fed in two orthogonal crystal directions, as indicated in Fig. S20a,b. In this arrangement, current either passes along or across crystal steps which exist as a result of substrate preparation. The data for perpendicular field orientation is plotted in panel c. In GaAs it has been seen that tilting the 2DES can induce a charge density wave ground state and/or rearrange its spatial orientation^{29,30}. Throughout this work, the current I is applied parallel to the $[11\bar{2}0]$ crystal direction. This crystal direction is in turn aligned perpendicular to the in-plane magnetic field applied when tilting the sample. In panel d, transport data for $\theta = 44^\circ$ well beyond the first coincidence position are shown. In this arrangement too, despite the significant in-plane magnetic field, no clear anisotropic behavior is observed.

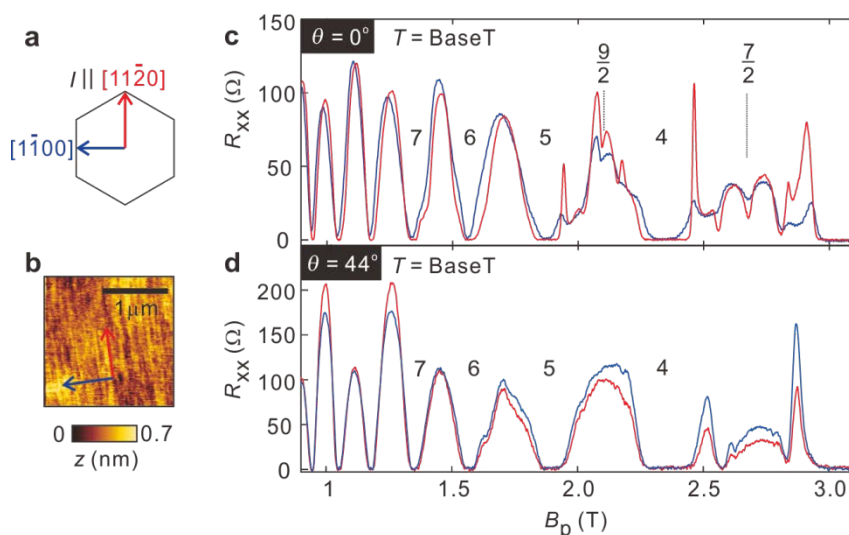


Figure S20: Current direction dependent magnetotransport in higher index LLs. **a**, Schematic showing the current orientation relative to the ZnO c -plane and **b**, the surface morphology as measured by atomic force microscopy of the heterostructure under investigation. **c**, Transport for two orthogonal current directions when the sample is only exposed to a perpendicular magnetic field. **d**, Same as before except the sample is now tilted to $\theta = 44^\circ$.

Even for higher tilt angles when the system has entered the highly spin polarized regime and screening is significantly less effective, we still observe a lack of anisotropy, as shown in Fig. S21. While this regime displays an inclination for reentrant quantum Hall behavior and localization, such behavior is essentially isotropic. In this plot it is apparent that the feature at $\nu_e = 4/3$ exists as a shoulder on the resistance for the red trace, and a weak minimum in the blue trace.

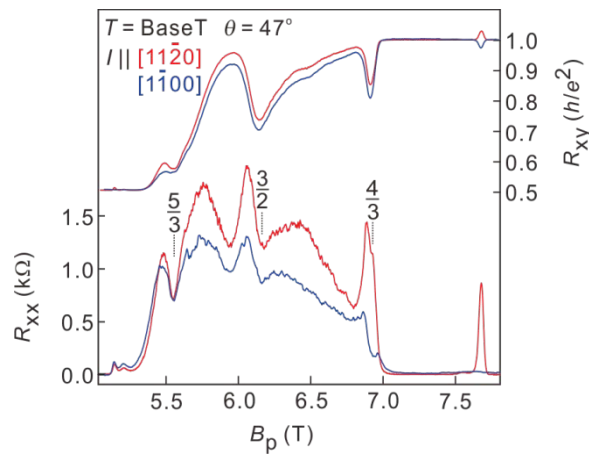


Figure S21: Current direction dependent magnetotransport around $\nu_e = 3/2$ at a tilt angle $\theta = 47^\circ$.

Supplementary References:

34. Nakano, M. *et al.* Electronic-Field Control of Two-Dimensional Electrons in Polymer-Gated–Oxide Semiconductor Heterostructures. *Adv. Mater.* **22**, 876-879 (2010).
35. Betancourt, J. *et al.* Polarization discontinuity induced two-dimensional electron gas at ZnO/Zn(Mg)O interfaces: A first-principles study. *Phys. Rev. B* **88**, 085418 (2013).
36. Dean, C. R. *et al.* Contrasting Behavior of the 5/2 and 7/3 Fractional Quantum Hall Effect in a Tilted Field. *Phys. Rev. Lett.* **101**, 186806 (2008).
37. Kozuka, Y. *et al.* Single-valley quantum Hall ferromagnet in a dilute $\text{Mg}_x\text{Zn}_{1-x}\text{O}/\text{ZnO}$ strongly correlated two-dimensional electron system. *Phys. Rev. B*, **85**, 075302 (2012).
38. Maryenko, D., Falson, J., Kozuka, Y., Tsukazaki, A. and Kawasaki, M. Polarization dependent Landau level crossing in a two-dimensional electron system in a MgZnO/ZnO -heterostructure, *Phys. Rev. B* **90**, 245303 (2014).
39. Maryenko, D. *et al.* Temperature-Dependent Magnetotransport around $\nu=1/2$ in ZnO Heterostructures, *Phys. Rev. Lett.* **108**, 186803 (2012).
40. Manoharan, H. C., Shayegan, M. and Klepper, S. J. Signatures of a Novel Fermi Liquid in a Two-Dimensional Composite Particle Metal. *Phys. Rev. Lett.* **73**, 3270-3273 (1994).
41. Du, R. R. *et al.* Drastic Enhancement of Composite Fermion Mass near Landau Level Filling $\nu = 1/2$. *Phys. Rev. Lett.* **73**, 3274-3277 (1994).
42. Park, K. and Jain, J. K. Phase Diagram of the Spin Polarization of Composite Fermions and a New Effective Mass. *Phys. Rev. Lett.* **80**, 4237-4240 (1998).
43. Liu, Y. *et al.* Multicomponent fractional quantum Hall states with subband and spin degrees of freedom. Preprint at <http://arxiv.org/abs/1501.06958> (2015).
44. Bishop, N. C. *et al.* Valley Polarization and Susceptibility of Composite Fermions around a Filling Factor $\nu=3/2$. *Phys. Rev. Lett.* **98**, 266404 (2007).
45. Simon, S. H. Comment on “Evidence for an Anisotropic State of Two-Dimensional Electrons in High Landau Levels”. *Phys. Rev. Lett.* **83**, 4223 (1999).